RSC Advances

PAPER

View Article Online
View Journal | View Issue

Cite this: *RSC Adv.*, 2024, **14**, 29330

Fabrication and characteristics of new quaternized chitosan nanocapsules loaded with thymol or thyme essential oil as effective SARS-CoV-2 inhibitors†

Nashwa M. Mahmoud,[a] Abdel Moneim Y. Abdel Moneim,[a] Omeed Darweesh,[b] Enas I. El Zahaby,[c] Reda F. M. Elshaarawy, *[a] Yasser A. Hassan[bc] and Mohamed G. Seadawy[d]

This research explores the potential of encapsulating thyme essential oil (TEO) and thymol (TH) into quaternized chitosan nanocapsules to combat SARS-CoV-2. Initially, the bioactive materials, TH and TEO, were extracted from *Thymus vulgaris* and then structurally and phytochemically characterized by spectral and GC-MS analyses. Meanwhile, *O*-quaternized ultrasonic-mediated deacetylated chitosan (QUCS) was successfully synthesized and characterized. Lastly, nanobiocomposites (NBCs; NBC1 and NBC2) were fabricated using QUCS as a scaffold to encapsulate either TEO or TH, with the mediation of Tween 80. By encapsulating these bioactive materials, we aim to enhance their efficacy and targeted delivery, bioavailability, stability, and anti-COVID properties. The new NBCs were structurally, morphologically, and physically characterized. Incorporating TEO or TH into QUCS significantly increased ZP values to ±53.1 mV for NBC1 and ±48.2 mV for NBC2, indicating superior colloidal stability. Interestingly, Tween 80-QUCS provided outstanding packing and release performance, with entrapment efficiency (EE) and loading capacity (LC) values of 98.2% and 3.7% for NBC1 and 83.7% and 1.9% for NBC2. The findings of *in vitro* antiviral studies not only highlight the potential of these nanobiocomposites as potential candidates for anti-COVID therapies but also underscore their selectivity in targeting SARS-CoV-2.

Received 4th May 2024
Accepted 8th September 2024

DOI: 10.1039/d4ra03298e

rsc.li/rsc-advances

1. Introduction

The novel coronavirus, SARS-CoV-2, has significantly impacted the world and will continue to do so in the foreseeable future. Since its initial outbreak in December 2019, it has rapidly spread across the globe, resulting in the development of a deadly respiratory illness known as COVID-19.[1,2] It has wreaked havoc on public health as it had a significant impact on morbidity and mortality in cases of a severe acute respiratory syndrome (SARS) and other complications, brought the global economy to a standstill and made the development of effective vaccines and medications an urgent priority. Nevertheless, SARS-CoV-2 antibiotic resistance is a significant challenge faced by healthcare providers. The research community is working hard to develop new tools and strategies to address this challenge.[3,4]

Recently, the use of essential oils (EOs) for fighting and treating SARS-CoV-2 is gaining attention in the medical community as an effective and safe option for treating the virus. Extensive research on this topic have found that EOs from various plants have exhibited antiviral activity against SARS-CoV-2, including EOs from clove, sweet basil, lemon balm, eucalyptus, tea tree, oregano, lemongrass, and rosemary oils.[5–8] For example, 38 adult COVID-19 patients who were not vaccinated for SARS-CoV-2 were treated in a clinical proof-of-concept (PoC) intervention study using a mixture of three aromatic plants' essential oils (CAPeo): Thymbra capitata (L.) Cav., *Origanum dictamnus* L., and Salvia fruticose Mill. Two groups of patients were formed from this sample: IG2020 (n = 13) and IG2021/22 (n = 25). The CAPeo treatment successfully reduced patient symptoms in 50% of cases in 2021 and 2022 and in 100% of cases in 2020.[9] While research is ongoing, it is worth noting that *in vitro* studies have indicated that thyme essential oil (TEO) could be a potential and effective remedy for fighting SARS-CoV-2.[10–12] Furthermore, thyme oil has antiviral and antimicrobial properties which may inhibit the virus's ability to

[a]*Department of Chemistry, Faculty of Science, Suez University, 43533 Suez, Egypt. E-mail: reda.elshaarawy@suezuniv.edu.eg*

[b]*College of Pharmacy, Al-Kitab University, Kirkuk 36015, Iraq*

[c]*Department of Pharmaceutics, Faculty of Pharmacy, Delta University for Science and Technology, Gamasa, Egypt*

[d]*Main Chemical Laboratories, Egypt Army, Cairo 11351, Egypt*

† Electronic supplementary information (ESI) available. See DOI: https://doi.org/10.1039/d4ra03298e

replicate, as well as help reduce inflammation and regulate the immune system. In addition, the authors noted that it could be used to reduce the severity of symptoms associated with COVID-19, such as fever, cough, and fatigue, and potentially reduce the duration of the illness. While further research is needed to confirm these results, the findings of some recently reported studies suggest that thyme oil may be a promising therapeutic agent in treating and preventing SARS-CoV-2 (COVID-19).[10–12] Despite the promising antiviral activity of TEO against several viruses, including influenza, herpes simplex, HSV-1, Coxsackievirus B3 (CVB3), and adenovirus, the widespread use of thyme oil as an antiviral medicine is still limited due to regulatory barriers. These barriers include its limited solubility, cytotoxic effects on human cells when taken in large doses, genotoxic effects, and skin irritation when applied topically.[13,14] Therefore, further research aimed at improving its solubility, delivery, and formulations, could allow its safe and efficient application in biomedicine.

Encapsulation of EOs by biopolymers has been found to offer a promising strategy for improving their stability and improving convenience in their applications. This strategy is based on the use of natural biopolymers such as proteins, lipids, and polysaccharides, to coat the EOs, which confers protection against environmental and biological influences, increases their shelf life, reduces volatility and potential odor issues, and enhances the release profile. Additionally, these biopolymers can act as emulsifiers, maintaining the stability of the formulation, and can even enhance the solubility, making the EOs more acceptable for a diverse range of uses.[15,16] Therefore, encapsulation of EOs by biopolymers is a promising strategy for improving the stability, applicability and overall effectiveness of EOs.

Many studies demonstrated that encapsulation of thyme essential oil with chitosan or its composites has proven to be an effective approach to tackle the aforesaid challenges. For instance, the encapsulation of TEO in chitosan nanoparticles (CSNPs) (nanocapsules) significantly increased its stability *via* the formation of protective hydrophilic chitosan layers around the TEO drops, preventing oxidation and evaporation, and thus increasing their solubility and stability as well as preserving the oil's beneficial properties.[17,18] Moreover, the antimicrobial,[18–20] antioxidant,[21] and antiviral[22] potentials of TEO significantly promoted following encapsulation by CSNPs. Meanwhile, numerous studies have shown that TEO's antimicrobial,[23–26] antioxidant,[27,28] anti-inflammatory,[29,30] and anticancer[30] properties are greatly enhanced when encapsulated within CS-based composites and nanocomposites, indicating that the encapsulation process had improved the bioavailability of the TEO. These results demonstrate that encapsulation of TEO with CS architectures is a promising approach for medical applications, as it can not only effectively protect the oil, but also increasing its stability and controlled release properties. However, to date, no study has been carried out on the creation and development of TEO-loaded CS-based nanocapsules intended to enhance antiviral or anti-COVID applications.

In light of these remarkable facts and our ongoing commitment to the discovery and development of novel, safe pharmacological systems,[31–34] we set out to test the capacity of a new chitosan derivative, *O*-quaternized ultrasonic-mediated deacetylated chitosan (QUCS), to encapsulate TEO or thymol (TH) and thereby enhance its bioavailability, stability, and anti-COVID properties.

2. Materials and methods

Specifications and sources for the commercial materials, reagents, and solvents utilized in this study were disclosed in the ESM.† Moreover, the synthesis methodology for *N*-benzylidene chitosan (CSB) was clearly explained in ESM.† The ESM† also includes a detailed description of the instruments used in the thorough characterization of the prepared materials. The ultrasound-assisted deacetylated squid chitosan (UCS) (average molecular weights (M_v) 1.01×10^6 g mol^{-1}, degree of polymerization (DP_v) 6188, and degree of acetylation (DA) 4.87%) used in this study was sourced from our previous work.[35]

2.1. TEO extraction

2.1.1. Plant material. The fresh aerial parts of *Thymus vulgaris* L. were collected from the desert of the North Sinai Governorate, Egypt, from October to December 2021 and identified by Prof. Dr Ibrahim Mashaly, Botany Department, Faculty of Science, Mansoura University. These plant specimens were air-dried and subsequently frozen until further processing.

2.1.2. Oil extraction. Following the methodology adopted by the Egyptian Pharmacopoeia,[36] 300 g of dried thyme plants were submerged in 3 L of distilled water and hydro-distilled for 3 h using a Clevenger-type apparatus (borosilicate glass with a 1000 mL flask, a 300 mm condenser, a 10 mL graduated Clevenger capacity, and joint dimensions of 24/29 mm). After separating the upper oil layer from the water, it was dried over Na_2SO_4 anhydrous and stored in airtight glass vials at 4 °C until further use.

2.1.3. GC-MS analysis. To determine the chemical make-up of the extracted TEO, we used a gas chromatograph-mass spectrometer (GC-MS) setup, with a Varian GC connected to a Finnigan SSQ 7000 Mass Selective Detector (MSD) running on the ICIS V2.0 data system (see ESM†).

2.1.4. Thymol isolation. Thymol was extracted from TEO using the protocol adapted by Bermejo *et al.*[37]

2.2. Preparation of QUCS

Fig. 1 shows the modified methodology used to prepare QUCS, which was adapted from earlier work.[38,39]

2.2.1. Preparation of *O*-quaternized-*N*-benzylidene chitosan (QBUCS). A method modified from a previously reported work[40] was used to prepare *O*-QBUCS by grafting quaternary ammonium groups onto BUCS surface. Briefly, a mixture containing 1.5 g of BUCS and 9.345 g (61.5 mmol) of glycidyltrimethylammonium chloride (GTMAC) dispersed in 100 mL of isopropanol was stirred at 70 °C for 30 h. After adding acetone to the reaction mixture, the intended product (*O*-QBUCS) was precipitated; the product was then filtered, washed thoroughly with acetone followed by ethanol solution (95%), and dried under vacuum at 50 °C for 24 hours.

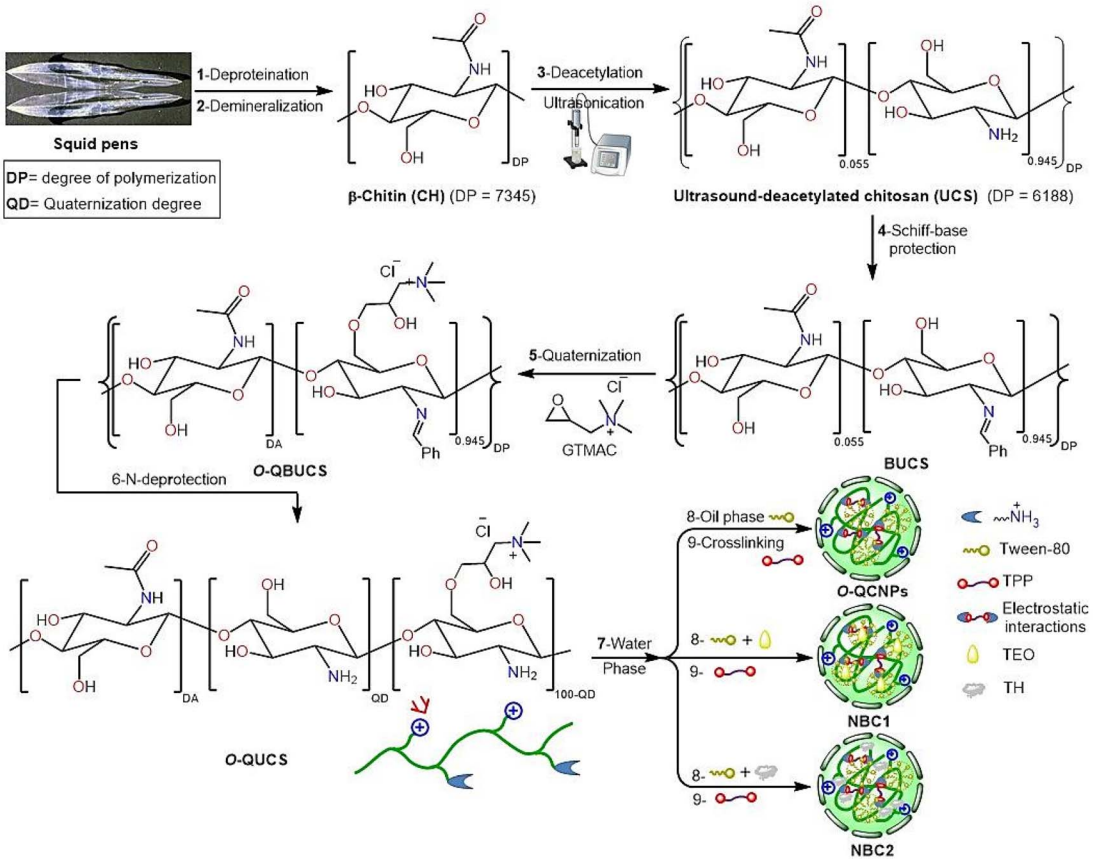

Fig. 1 Schematic pathways for the formulation of new nanobiocomposites.

2.2.2. Preparation of *O*-quaternized-chitosan (QUCS). QUCS was dispersed in 100 mL of an ethanolic HCl solution (0.25 mol L^{-1}) and the resulting dispersion was agitated for 24 h at room temperature. Afterward, an aqueous 1% Na_2CO_3 solution was used to neutralize the combination. The intended product was filtered and rinsed to a neutral pH after being precipitated with acetone. Pure QUCS was obtained by dissolving the obtained precipitate once again in distilled water, dialyzing against distilled water for three days, then lyophilizated at −50 °C, and finally drying under vacuum at 40 °C for 48 hours. By employing the $AgNO_3$ deposit-titration method, we were able to estimate the quaternization degree (QD),[41] and its value may be determined with the help of eqn (1):

$$QD\% = \frac{C_{AgNO_3} \times V_{AgNO_3}}{C_{AgNO_3} \times V_{AgNO_3} + \left(W - C_{AgNO_3} \times V_{AgNO_3} \times M_2\right)/M_1} \quad (1)$$

C_{AgNO_3} (mol L^{-1}) and V_{AgNO_3} (mL) are the molarity and volume of standard $AgNO_3$ solution, respectively; W is the weight of QUCS (g); M_1 and M_2 are the molar masses (g mol^{-1}) of the glucosamine and structural units in QUCS, respectively.

2.3. Preparation of QUCS-based nanobiocomposites (NBCs)

The ionic gelation method[42] was used to prepare the blank QUCS nanoparticles (QUCS) and their NBCs. In brief, microemulsion droplets combining CS, TEO or TH, and Tween 80 were first formed by the oil-in-water emulsion technique, and then the droplets solidification was achieved by crosslinking with tripolyphosphate (TPP) solution. To do this, a water phase was first prepared by dissolving QUCS in an aqueous acetic acid solution (1% (v/v), 3 mg mL^{-1}) and agitating the mixture at 300 rpm for 1 hour at 25 °C. After adjusting the QUCS solution's pH to 4.6 with 1 N NaOH under stirring for 30 min, it was combined with the pre-prepared oil phase incorporating TEO or TH (5.9 mg mL^{-1}) and Tween-80 (3 mg mL^{-1}) while stirring (500 rpm) at 42 °C and kept for 2 h at these conditions to generate a homogenous O/W microemulsions. Thereafter, while being stirred at 1000 rpm, these microemulsions were added dropwise to a TPP solution (0.75 mg mL^{-1}) using a peristaltic pump. For the microdroplets to crosslink and form the intended solidified NBCs, they were agitated at 500 rpm for 60 min. Following the stirring, the produced NBCs were gathered by centrifugation at 10 000 rpm for 35 min at 4 °C, followed by repeated washes with distilled water. They were then re-dispersed in deionized water while being sonicated for 15 s, then freeze-dried for an entire night at −20 °C. The blank (control) nanoparticles were prepared using the same method but in the absence of TEO and TH.

2.4. Encapsulation efficiency (EE) and loading capacity (LC)

Spectrophotometric measurements at 275 nm were performed using a previously described methodology[30] to determine the amount of TEO or TH entrapped in the QUCS (encapsulation efficiency, EE), as well as the amount of TEO or TH loaded per unit weight of QUCS (loading capacity, LC). The findings of each experiment were performed in triplicate and reported as mean ± SD. The following formulas (eqn 2 and 3) were used to compute the EE and LC:[30]

$$\mathrm{EE}\% = \frac{\text{amount of TEO entrapped}}{\text{initial amount of TEO or TH}} \times 100 \quad (2)$$

$$\mathrm{LC}\% = \frac{\text{amount of TEO or TH entrapped}}{\text{initial amount of QUCS}} \times 100 \quad (3)$$

2.5. *In vitro* TEO release

The *in vitro* release of TEO or TH from QUCS at 37 °C was examined in three different simulated fluids: simulated gastric fluid (SGF) (pH = 1.2), simulated intestinal fluid (SIF) (pH = 6.8), and simulated colonic fluid (SCF) (pH = 7.4) according a protocol used in our previous work.[43] Briefly, 3 mg of each NBC was dispersed in 3 mL of simulated fluid before being dialyzed at 37 °C for 72 hours in a dialysis bag (MWCO 1 kDa) submerged in 90 mL of release medium. 3 mL samples of the releasing media were taken at regular intervals, and their TEO concentration was estimated by spectrophotometric analysis at 279 nm. After withdrawing each sample, the releasing medium was reconstituted with 3 mL of the parent simulated fluid. A calibration graph between absorbance and TEO or TH content was used to quantify the release concentration. The cumulative release (CR) of TEO or TH from QUCS was calculated using the following equation (**eqn 4**):

$$\mathrm{CR}\% = \sum_{t=0}^{t} \frac{m_t}{m_0} \times 100 \quad (4)$$

m_0 and m_t are initial and released amounts of TEO or TH at time t (min).

2.6. Biological studies

2.6.1. Cell culture and virus stock. The SARS-CoV-2 viral cells (EGY/WAT-2 VACCERA) and Vero E6 cells (ATCC CCL-8) were donated by the Virology Sector, VACSERA (Giza, Egypt). Dulbecco's Modified Eagle's Medium (DMEM) supplemented with 10% Fetal Bovine Serum (FBS) and 1% Penicillin/Streptomycin (pen/strep) antibiotic mixture was used to cultivate Vero-E6 cells at 37 °C and 5% CO_2. The SARS-CoV-2 virus stock was prepared in Vero cell culture. To prepare a virus stock, we seeded cells into tissue culture flasks 24 hours before infection with the SARS-CoV-2 viral cells (EGY/WAT-2 VACCERA) in an infection medium (DMEM with 2% FBS, 1% pen/strep, and 1% L-1-tosylamido-2-phenylethyl chloromethyl ketone [TPCK]-treated trypsin) at a multiplicity of infection (MOI) of 0.1. After 2 hours of incubation, the virus-inoculum-containing infection medium was transferred to new media and incubated for 3 days. The cell supernatant was centrifuged for 5 min at 2500 rpm and strained to extract minute particle debris from the cells at the specified time. The 50 mL falcon tube was used to transfer the supernatant. It was then divided into smaller portions, and the plaque infectivity assay was used for titration.

2.6.2. Cytotoxicity. Following the protocol described by Mustafa *et al.*,[44] the MTT test was used to assess the cytotoxicity of novel formulations towards Vero E6 cells. The cytotoxicity percentage was calculated using formula (**eqn 5**). The half maximal cytotoxic concentration (CC_{50}) was determined by plotting the percentage of cytotoxicity against the concentration of the sample.

$$\text{Cytotoxicity}\% = \left(\frac{\text{absorbance of untreated cells} - \text{absorbance of treated cells}}{\text{absorbance of untreated cells}}\right) \times 100 \quad (5)$$

2.6.3. Plaque infectivity assay. The plaque infectivity assay used a slightly modified version of a previously published work[45] to titrate SARS-CoV-2 viral cells (EGY/WAT-2 VACCERA). Briefly, the virus was diluted in a series of ten-fold dilutions using an FBS-free medium. Thereafter, the 80–90% confluent Vero-E6 cell monolayers were inoculated using a mixture of 400 μL of infection media and 100 μL of each viral dilution. A separate well in the same plate was used as a control and was seeded with 500 μL of a serum-free medium. After that, the plate was placed in an incubator set at 37 °C with CO_2 (5%) for 1 hour to let the virus adsorb. Every 15 min, it was shaken to make sure the cells were exposed evenly to the infection and to keep them from drying up. Once the virus inoculum had been incubated for 1 h, it was removed and the cell monolayers were covered with 3 mL of DMEM with 0.6% agarose, 1 μg mL^{-1} of TPCK-treated trypsin, 10% FBS, 1× pen/strep, and the tested sample. After 10 min at room temperature (RT), the plate was placed in an incubator at 37 °C with 5% CO_2 to enable the agarose content to solidify. Following 72 h, each well was treated with 1 mL of a fixation solution containing 10% formalin for 1 hour in order to fix the cells and inactivate the virus. The fixer was thereafter removed, and the plate wells were rinsed with water and allowed to dry. Each well was stained with 1 mL of the 0.1% crystal violet staining solution for 5 min. After that, the dye was removed, and the plate wells were rinsed with water and dried to allow for visualization of the plaques. Clear, unstained dots on a violet backdrop (stained cells) were the hallmarks of viral plaques. The following equation (**eqn 6**) was used to determine the viral titer, plaque-forming unit (PFU) per mL:

$$\text{PFU per mL} = \text{number of plaques} \times \text{inoculated virus volume} \times \text{virus dilution} \times 10 \quad (6)$$

2.6.4. Plaque reduction assay. The plaque reduction experiment was performed in a six-well plate with Vero-E6 cells

(1.2×10^6 cells) cultured for 24 hours at 37 °C to evaluate the initial antiviral activity of the novel nanoformulations. After diluting the viral cells to 10^2 PFU/well, they were combined with the tested drugs at a safe concentration and incubated at 37 °C for 1 hour before being administered to the cells. Following the removal of growth medium from the culture plates, the cells were injected with 100 μL per well of virus along with the examined nanoformulations. Following one hour of virus adsorption, the cell monolayers were treated with 3 mL of DMEM that had been supplemented with the overlay medium containing the tested samples. After being left to solidify, the plates were placed in an incubator set at 37 °C for three days, or until viral plaques formed. Before staining the plates with 0.1% crystal violet (CV) in distilled water, the cell fixing solution was applied and left for 1 hour. Untreated virus was incubated with Vero-E6 cells in control wells; plaques were then counted, and the following formula (eqn 7) is used to estimate the percentage reduction in plaque development compared to control wells:

$$\text{Reduction } \% = \left(\frac{\text{untreated virus count} - \text{treated virus count}}{\text{untreated virus count}}\right) \times 100 \quad (7)$$

2.6.5. Inhibitory concentration 50 (IC_{50}) determination. 2.3×10^4 Vero-E6 cells were evenly distributed in each well of 96-well tissue culture plates. The plates were then placed in a humidified 37 °C incubator with 5% CO_2 overnight. Afterward, the cell monolayers were washed once with 1× PBS and left to undergo virus adsorption at RT for an hour. Extra 50 μL of DMEM with different doses of the investigated substances was then added on top of the cell monolayers. Once the cells had been incubated for 72 h at 37 °C in a 5% CO_2 incubator, they were fixed for 20 min with 100 μL of 4% paraformaldehyde. Then, they were stained with CV (0.1%) in distilled water for 15 min at RT. After dissolving the CV dye in 100 μL of absolute methanol per well, the Anthos Zenyth 200 RT plate reader was used to quantify the color's optical density at 570 nm. The IC50 of the substance is the concentration needed to decrease the viral-induced cytopathic effect (CPE) by 50%, compared to the virus control.

2.7. Statistical analysis

Each experiment was repeated three times, and the final results were reported as the mean ± SD. Findings were graphed using OriginPro 9.1 software. One-way analysis of variance (ANOVA) (SPSS v. 22, USA) was used to complete the necessary statistical analysis, and Tukey's multiple comparison post-hoc tests was then used to make the necessary pairwise comparisons. Significant differences were defined as those with P values lower than 0.05.

3. Results and discussion

3.1. Extraction and characterization of TEO

The Thyme essential oil (TEO) was obtained from *Thymus vulgaris* L. by the conventional hydrodistillation (HD) method. Table 1 presents a comprehensive enumeration of the chemical constituents discovered in the thyme aerial parts' TEO, which was extracted using the HD method.

The 45 components enumerated in Table 1 account for 99.12% of the cumulative peak areas observed in the GC chromatogram. The primary constituents found in the TEO include phenolic compounds such as Thymol and Carvacrol, sesquiterpene Germacrene D, as well as oxygenated sesquiterpenes like α-Acorenol and D-Germacren-4-ol. It is worth noting that over 75% of the constituents present in TEO consist of oxygenated molecules.

3.2. Synthesis protocol

Initially, ultrasound-assisted deacetylated chitosan (UCS) was prepared by subjecting chitin isolated from squid pen wastes by our standard extraction methodology (deproteinization (DP) subsequent to demineralization (DM)) to an ultrasound-assisted deacetylation (UDA) process.[35] After that, the *O*-quaternized ultrasound-assisted deacetylated chitosan (QUCS) was synthesized by *O*-quaternization of UCS with glycidyl *N*,*N*,*N*-trimethyl ammonium chloride (GTMAC) through three sequential reactions: Schiff-base condensation with benzaldehyde to protect the NH_2 group, *O*-quaternization with GTMAC, and subsequent NH_2 deprotection under acidic hydrolysis conditions. To synthesize the TEO-loaded QUCS nanocapsule (NBC1) and TH-loaded QUCS nanocapsule (NBC2), the OOPE or TH compound was entrapped within the QUCS network through the initial preparation of an oil/water (O/W) emulsion, which was subsequently subjected to an ionic gelation procedure. The O/W emulsion was initially created by combining the oil phase consisting of TEO/DCM/tween-80 with an aqueous phase containing QUCS solution in AcOH (1% v/v). This mixture was subsequently subjected to an ionic gelation process facilitated by an aqueous TPP solution (see Fig. 1).

3.3. Physicochemical and morphological characterization

3.3.1. Zeta potential (ZP). Zeta potential is a crucial parameter in the characterization of nanocomposites due to its significant impact on their stability, aggregation, and interaction with biological systems. As Zhang *et al.* (2008) reported, zeta potential is defined as the electrical potential difference at the slipping plane between the particle surface and the surrounding fluid medium. It reflects the surface charge of nanocomposites and is influenced by factors such as pH, ionic strength, and surface functionalization. The zeta potential's magnitude and sign determine nanocomposites' stability in suspension. Nanocomposites with high absolute zeta potential values (ZP ≥ ± 30 mV) are more stable due to the increased electrostatic repulsion between particles, preventing agglomeration and maintaining colloidal stability. On the other hand, nanocomposites with low zeta potential values are prone to aggregation, leading to decreased stability and potential loss of their desired properties. Moreover, zeta potential plays a crucial role in the interaction of nanocomposites with biological systems. The zeta potential of nanocomposites affects their cellular uptake, biodistribution, and toxicity. For example,

Table 1 Phytochemical composition of the isolated TEO

No.	Compound	RT (min)	Yield (%)	No.	Compound	RT (min)	Yield (%)
Phenolic constituents				24	Isolongifolene oxide	19.72	0.83
1	Thymol	9.21	8.32	25	Alloaromadendrane-4β,10α-diol	19.86	0.57
2	Carvacrol	9.51	6.96	26	(−)-Spathulenol	20.24	0.61
Hydroxyl and terpenoid constituents				27	Cembrene	21.13	0.82
3	*p*-Mentha-1-ene-6-one	9.59	0.64	28	Isolongifolene oxide	20.51	0.61
4	Cubebanol	12.67	4.47	29	Thunbergol	21.43	0.59
5	α-Acorenol	13.30	6.25	30	Cyclooctenone dimer	18.92	0.57
6	(−)-Globulol	13.39	4.75	Terpenes			
7	Junenol	13.42	1.15	31	*o*-Cymene	6.92	0.45
8	6-Epi-shyobunol	13.67	0.65	32	α-Copaen	10.19	3.86
9	D-Germacren-4-ol	14.31	5.61	33	α-Yalangene	10.32	0.55
10	Cubebanol	14.48	0.74	34	(−) β-Elemene	10.56	1.85
11	τ-Muurolol	15.53	1.68	35	Germacrene A	10.69	1.35
12	τ-Cadinol	15.79	1,04	36	α-Gurjunen	10.85	0.88
13	α-Cadinol	15.97	1.75	37	Isocaryophillene	11.07	3.58
14	Carotol	16.57	7.60	38	Humulene	11.79	4.12
15	α-Acorenol	13.30	6.25	39	Germacrene D	12.43	10.10
16	6-Epi-shyobunol	16.74	0.81	40	D-Guaiene	12.85	0.57
17	Ledol	16.85	0.56	41	Longifolenaldehyde	18.14	0.53
18	α-Pinene oxide	16.91	1.69	42	2,4-Patchouladiene	18.19	3.09
19	Caryophyllene oxide	18.02	1.31	43	8,9-Dehydro-cycloisolongifolene	18.32	0.75
20	Cholestan-3-ol	18.68	1.22	Esters			
21	Nonadecatriene-5,14-diol	18.75	0.71	44	Aristol-1(10)-en-9-yl isovalerate	18.28	0.75
22	Ledene oxide-(II)	19.49	2.03	45	Nerolidol-epoxyacetate	18.56	1.05
23	(−)-Spathulenol	19.57	1.03				

positively charged nanocomposites with high zeta potential interact more strongly with negatively charged cell membranes, enhancing cellular internalization. Conversely, negatively charged nanocomposites with low zeta potential may exhibit reduced cellular uptake.[46] Therefore, controlling the ZP of nanocomposites is essential for optimizing their performance in various applications. In this context, the zeta potential values of new materials were measured at physiological pH (7.4) (see Fig. 2). The measurements showed that the QUCS had a highly positive ZP value (±36.4 mV), indicating a higher surface charge. This increased surface charge is attributed to the presence of quaternary ammonium groups on the nanocomposite surface, which provide positive charges. Furthermore, incorporating thyme extract or thymol into QUCS significantly increased the ZP value to ±53.1 mV for NBC1 and ±48.2 mV for NBC2. This increase in zeta potential indicates a change in the surface charge of the nanoparticles, which can have implications for their stability and interactions with biological systems. Through the process of encapsulation, essential oils are combined with quaternized chitosan. The chitosan molecules, which carry a positive charge, bind to the surface of the essential oil droplets. This leads to an overall increase in the positive charge of the system. Consequently, this results in an elevated positive zeta potential, enhancing the stability and dispersibility of the encapsulated essential oils.[22]

The physicochemical stability of the new nanocapsules (QUCS) and nanocomposites (NBC1 and NBC2) was evaluated by measuring the changes in their zeta potential (ZP) values over a one-week storage period in PBS under physiological circumstances. This evaluation is crucial because zeta potential serves as a fundamental indicator of the stability of colloidal substances. Throughout the monitoring period, it was noted that the ZP values of the nanocomposites were consistently steady (see Fig. 2C), suggesting strong resistance to aggregation and precipitation in PBS. The preserved ZP values indicate that these nanocomposites have inherent physicochemical stability when subjected to ionic intensities similar to physiological conditions.[30,47] The attribute mentioned highlights these materials' potential effectiveness and dependability for biomedical purposes, namely in drug delivery systems. In such applications, it is crucial for the materials to maintain long-term physical stability to preserve their functional integrity and ensure optimal therapeutic performance.

3.3.2. FTIR spectroscopy. The FTIR spectra of new materials provide preliminary proof for their successful formation and valuable information about their structural properties. In this context, several distinct absorption peaks can be seen in the QUCS spectrum (Fig. 3A and Fig. S1, ESM†), such as absorption bands observed around 3370 and 1594 cm^{-1}, which can be attributed to the stretching vibration of the N–H bond in quaternized chitosan. Another significant absorption band was observed at around 1654 cm^{-1}, corresponding to the stretching vibration of the C=O bond in the amide group. The presence of this absorption band indicates the successful quaternization of chitosan. Additionally, absorption bands at approximately 1450 cm^{-1} and 1370 cm^{-1} can be assigned to the bending vibration of the $-CH_2-$ group in quaternized chitosan. These absorption bands provide evidence of the successful incorporation of quaternary ammonium groups into the chitosan structure.[47,48] On the other hand, several significant peaks can

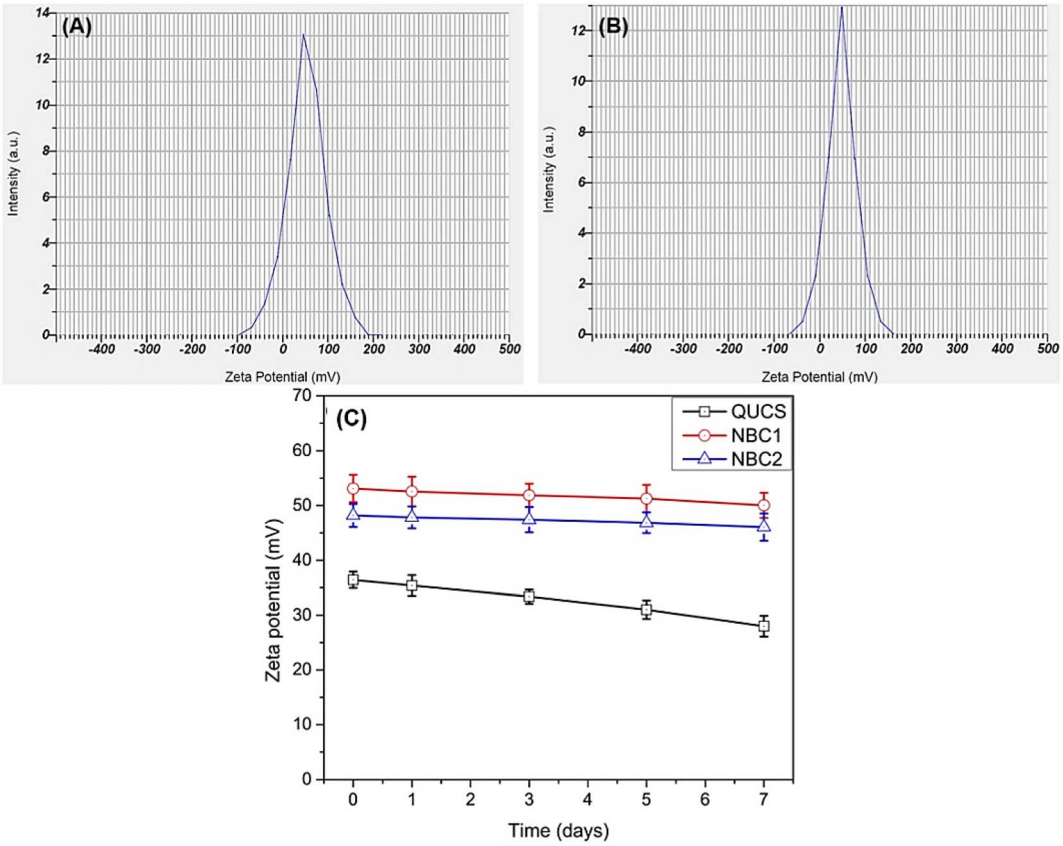

Fig. 2 Zeta potential values of new nanocomposites (A) NBC1, TEO-Tween 80-QUCS and (B) NBC2, TH-Tween 80-QUCS. (C) Physicochemical stabilities evaluation of new materials by monitoring their zeta potential (ZP) values changes over a one-week storage period in PBS.

be seen in the FTIR spectrum of thyme oil extract, which corresponded to specific functional groups. For instance, a strong peak observed at around 1710 cm^{-1} indicated the presence of carbonyl groups, which are commonly found in aldehydes, ketones, and carboxylic acids. This peak suggests the presence of compounds such as thymol and carvacrol, which are major constituents of thyme oil. Another notable peak was observed at approximately 2930 cm^{-1}, which is characteristic of the C–H stretching vibration of aliphatic hydrocarbons. This peak indicates the presence of terpenes, which are major components of thyme oil. Additionally, peaks at around 3037 cm^{-1} and 1580 cm^{-1} indicated the presence of aromatic rings, further confirming the presence of thymol and carvacrol.[30] The FTIR spectrum of thymol exhibited characteristic peaks at 3400 and

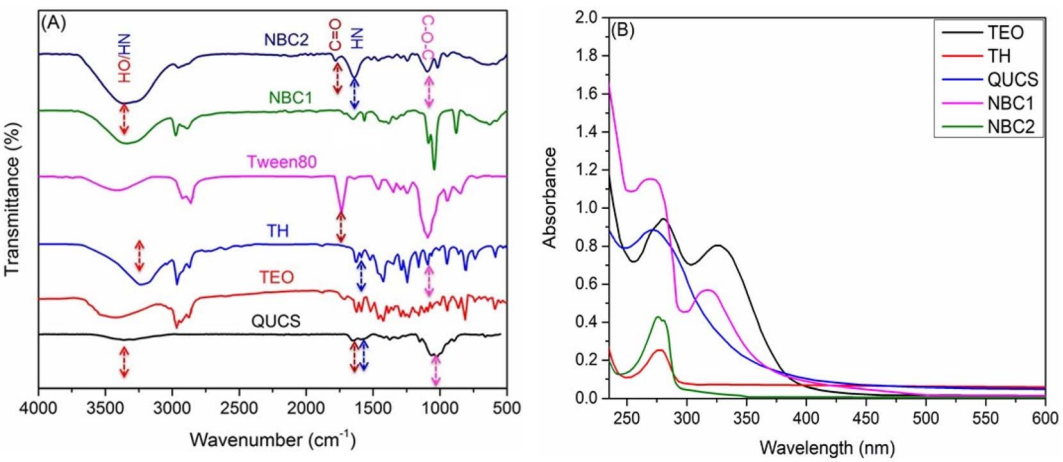

Fig. 3 (A) FTIR spectra of new nanocomposites (NBC1, TEO-Tween 80-QUCS; NBC2, TH-Tween 80-QUCS) and their native ingredients. (B) UV-vis spectra of TH, TEO, and NBC1.

3000–2850 cm^{-1} correspond to the stretching vibrations of O–H and C–H bonds, indicating the presence of hydroxyl and alkyl groups in the molecule. Additionally, the peaks at 1596 and 1454 cm^{-1} correspond to the stretching vibrations of the aromatic ring. The stretching vibrations of the O–H alcoholic, C–H olefinic, C–H methyleneic, and methyl groups may be seen as prominent peaks in the FTIR spectrum of Tween 80 at 3419, 3024, 2929, and 2859 cm^{-1}, respectively.[49] The ester fragment's carbonyl group (C=O) can be identified by an extremely strong stretch at 1733 cm^{-1}. As for the FTIR spectrum of NBC1 (TEO-Tween 80-QUCS), it integers the characteristic IR peaks of its native components (Fig. 3A), however, with remarkable changes in their spectral features owing to their mutual interactions. To name a few, aside from the major characteristic vibration peaks of TEO observed at 3340, 1619, and 1279 cm^{-1} assignable to aromatic ring and phenolic O–H, it can also be seen a strong peak at 1720 cm^{-1} due to the stretching vibration of ester C=O group Tween 80 as well as the main QUCS spectral peaks (3449 cm^{-1}, O–H and N–H; 1639 cm^{-1}, amide I (C=O); 1589 cm^{-1}, amide II (N–H); 1040 cm^{-1}, glycosidic bond (C–O–C)). This is indicative of the successful formulation of this nanobiocomposite. Similarly, the FTIR spectrum of NBC2 (TH-Tween 80-QUCS) confirms its successful formation as revealed by the emergence of IR peaks characteristic of the major functional groups of TH, Tween 80, and QUCS with remarkable changes in their positions and/or intensities due to their mutual interactions.

3.3.3. UV-vis spectroscopy. The UV-vis spectra of both pure thyme extract and QUCS that have been loaded with thyme extract (Fig. 3B) reveal some intriguing details about the nature of the interaction between the two substances. The thyme extract (TEO) exhibited absorbance peaks at 279 nm and 340 nm, suggesting the presence of aromatic compounds such as phenols and flavonoids. These compounds are known for their antioxidant properties and have been associated with various health benefits. On the other hand, the TEO-loaded QUCS (NBC1) displayed new absorbance peaks at 269 nm and 325 nm. This observation suggests that the QUCS interacted with the compounds present in the thyme extract, leading to changes in the absorption pattern.[50] The UV-vis spectrum of thymol-loaded chitosan nanoparticles (NBC2) exhibits a prominent absorption peak around 274 nm, attributed to the π–π^* transition of aromatic rings present in thymol. The encapsulation process generally results in a shift or broadening of a native thymol peak (279 nm) due to interactions between thymol and chitosan polymer chains, suggesting successful loading and stabilization.[51]

3.3.4. ^{1}H NMR spectroscopy. The ^{1}H NMR spectrum of QUCS confirms its successful formation and provides valuable insights into its structural characteristics. This NMR spectrum exhibits several distinct peaks that provide valuable information about the functional groups present in the QUCS. The ^{1}H NMR spectrum of QUCS (see Fig. S2, ESM†) exhibited distinct peaks at chemical shifts of 4.23 and 3.85 ppm, corresponding to the protons on the hydroxyl group of the chitosan backbone.[52] Another peak is observed at 3.70 ppm, attributed to the protons on the *N*-acetyl group of chitosan. A set of peaks observed at the range of 3.63–3.44 ppm could be attributed to the resonance of chitosan skeleton protons. A very sharp peak was noticed at 3.36 ppm, which is characteristic of the protons on the methyl group of the trimethyl ammonium chloride.[53] The high intensity of this peak indicates a high degree of substitution of the UCS.

3.3.5. Energy-dispersive X-ray spectroscopy (EDS) analysis. Intriguing details on the elemental composition and distribution of the nanobiocomposites (NBC1 and NBC2) can be seen in their EDS spectra (Fig. 4). The EDS spectra of both nanocomposites are almost identical and showed that carbon (C), oxygen (O), chlorine (Cl), and phosphorus (P) elements were indeed present in the EDS spectrum of the nanocomposite, however with varying ratios, indicating their incorporation into the nanocomposite structures. Low sample nitrogen concentration may explain the absence of a nitrogen peak in the EDS spectrum. A peak is detected *via* EDS spectroscopy, which requires enough of the element of interest. The EDS spectrum may not identify a nitrogen peak if the sample has too little nitrogen. During quaternization and encapsulation, chitosan amines are replaced with quaternary ammonium groups, followed by loading TEO (multiple N-free components) into the matrix of QUCS, reducing the nitrogen content to a non-detectable level. Another possible explanation for the absence of nitrogen in the EDS spectra could be the shielding effect of the oil loaded within the nanoparticles, preventing the detection of nitrogen signals by the EDS technique. These findings align with the results of previous investigations.[54–56]

3.3.6. Scanning electron microscopy (SEM) analysis. SEM scans were used to compare the morphology of NBC1 and NBC2 to that of QUCS. As can be seen in Fig. 5A, the micrograph obtained from SEM demonstrated that the QUCS possessed a predominantly smooth surface interspersed with areas exhibiting rough and porous textures. These porous areas are crucial in improving its drug loading efficiency. On the other hand, the SEM micrographs (Fig. 5B and C) obtained revealed that the nanocomposites exhibited semi-spherical hybrid with irregular shapes with smooth surfaces, highlighting the successful encapsulation of oil and TH within the matrix of QUCS nanoparticles. The well-dispersion of particles observed in these images can be attributed to various factors, including the high positive zeta potential values, which create a strong repulsive force between particles, preventing their aggregation and ensuring long-term stability. This repulsion is attributed to the nanoparticles' charged surface groups, which create an electric double layer that inhibits particle–particle interactions.[57] Additionally, incorporating surfactant (Tween 80) during the nanocomposites synthesis process resulted in the formation of protecting layer with a smooth surface. This can be attributed to the ability of surfactants to reduce the surface tension and stabilize the nanoparticles, facilitating the formation of a semi-spherical shape.[58]

3.4. Pharmacological characterization

3.4.1. Entrapment efficiency and loading capacity. Entrapment efficiency (EE), the percentage of TEO successfully

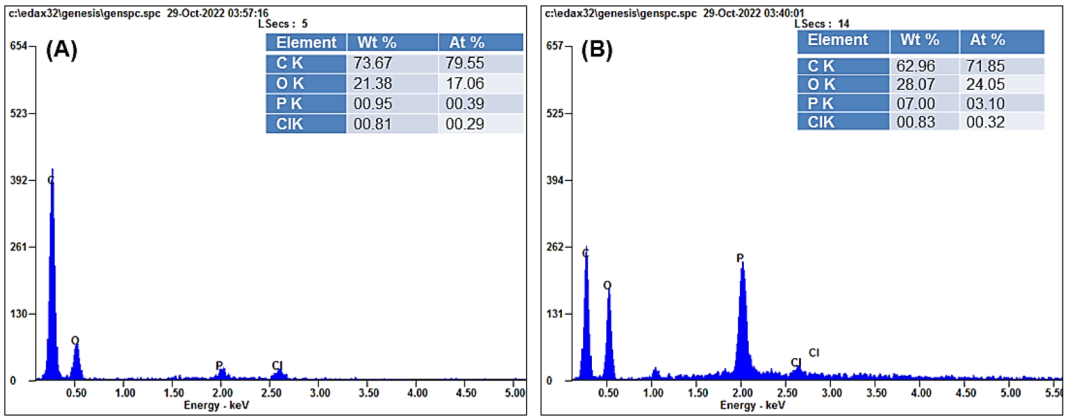

Fig. 4 Energy-dispersive X-ray spectroscopy (EDS) spectra of (A) NBC2, TH-Tween 80-QUCS and (B) NBC1, TEO-Tween 80-QUCS.

incorporated into the QUCS nanoparticles during the preparation process, and loading capacity (LC), the maximum amount of TEO that can be loaded into a given amount of QUCS nanoparticles, play vital roles in the drug encapsulation process within the pharmaceutical industry. These parameters are essential in ensuring the effective delivery and release of drugs to their intended targets. By optimizing EE and LC, pharmaceutical companies can improve the therapeutic efficacy of their drug formulations while minimizing potential side effects. In this context, the Tween 80-QUCS' packing properties for encapsulating TEO and TH were evaluated by calculating their respective EE and LC. Tween 80-QUCS has a remarkable potential for loading and encapsulating EOs as demonstrated by the quantification of the packing characteristics (EE and LC) of TEO-encapsulated Tween 80-QUCS nanocapsules (TEO-Tween 80-QUCS, NBC1) (see Table 2). These values are 98.2% and 3.7%, respectively. The negligible oil loss (1.8%) of TEO may have resulted from the volatile components of the oil evaporating during the encapsulation process. However, it was revealed that Tween 80-QUCS nanocapsules containing TH (TH-Tween 80-QUCS, NBC2) had an estimated EE of 83.7% and an LC of 1.9%. HT in NBC2 was present at a far higher concentration than in any other TH-based nanocapsules described to date,[59–61] revealing that Tween 80-QUCS has great potential for encapsulating and delivering TH and other natural antioxidant compounds.

3.4.2. *In vitro* release kinetics. Nanoparticle encapsulation has emerged as a pivotal strategy in enhancing essential oils' stability and controlled release. Encapsulating the oil within nanoparticles can significantly improve its stability, ensuring its efficacy and shelf-life are prolonged. Additionally, nanoparticle encapsulation enables a controlled release mechanism, allowing for sustained and targeted oil delivery. This controlled release not only enhances the efficiency of thyme oil but also minimizes potential side effects associated with its rapid and uncontrolled release.[21] TEO released from quaternized chitosan nanocapsules presents a fascinating phenomenon characterized by a three-phasic process. This process unfolds with an initial burst phase, followed by significantly reduced TEO release rates, culminating in a plateau phase where the maximum value (74%) is achieved after 24 h (see Fig. 6). The release of TEO from the QUCS is a multifaceted process affected by several factors. These factors include the composition of the release media, the interactions between the chitosan matrix and thyme oil, and the diffusion characteristics of the nanocapsules.[19] Upon exposure of the TEO-loaded QUCS (NBCs) to the release media (PBS), chitosan nanocapsules gradually released oil from their inner layers, resulting in solubilization. The subsequent step involved the swelling of the nanocapsules, resulting in the gradual release of the encapsulated thyme oil.[30] The release medium finally had enough time to infiltrate the

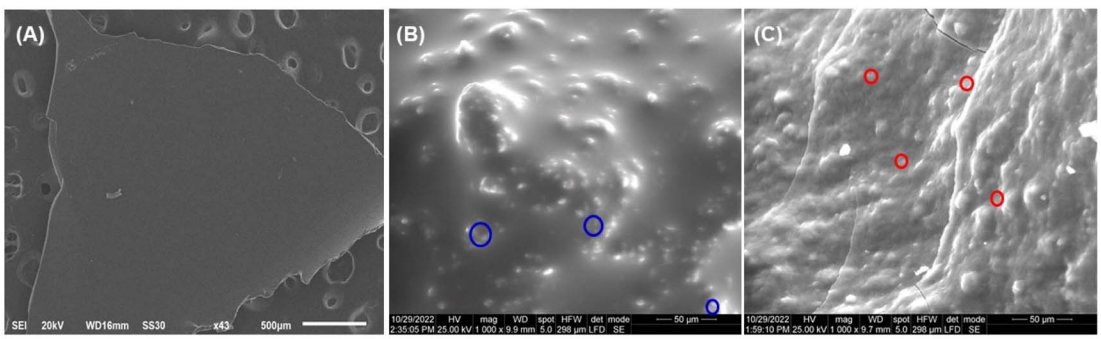

Fig. 5 SEM micrographs of (A) QUCS; (B) NBC1, TEO-Tween 80-QUCS; and (C) NBC2, TH-Tween 80-QUCS. The inside red and blue circles refer to the nanoparticulate structures of TEO-loaded QUCS and TH-loaded QUCS, respectively, in the obtained composite networks.

Table 2 CC_{50} and IC_{50} (μg mL^{-1}) as well as SI values of the obtained formulations against Vero E6 and SARS-CoV-2 cells, respectively, in comparison to a reference drug (ciprofloxacin, CIP)

Sample	TEO	TH	QUCS	NBC1	NBC2	CIP
ZP (mV)	—	—	±36.4	±53.1	±48.2	—
EE (%)	—	—	—	98.2	83.7	—
LC (%)	—	—	—	3.7	1.9	—
CC_{50} (Vero E6) (μg mL^{-1})	179.87	9.39	201.14	137.95	141.18	2923.33
IC_{50} (SARS-CoV-2) (μg mL^{-1})	0.885	3.143	0.96	0.026	0.33	48.26
SI	203.24	2.99	209.52	5305.77	4278.18	60.57

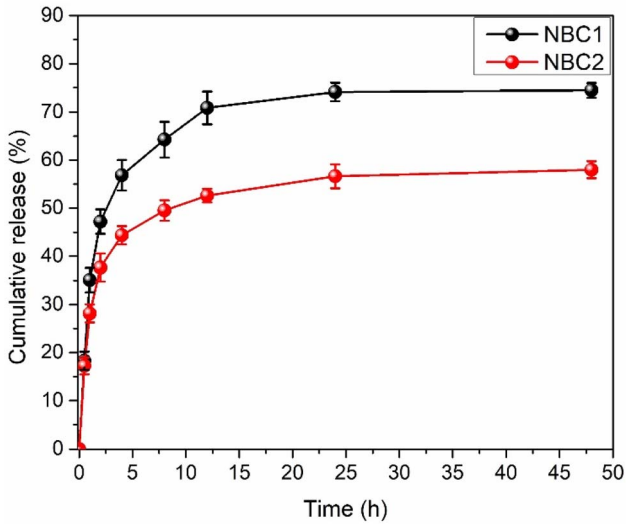

Fig. 6 Quantification of TEO and TH released *in vitro* under physiological conditions from their corresponding nanobiocomposites (NBC1 and NBC2, respectively).

nanocapsules' interior layers and reach equilibrium over time.[62] Similarly, it takes three phases to release TH from QUCS nanocapsules. The first stage entailed the fast release of loosely bound or near-surface thymol molecules. A thymol burst release may have increased the medium's thymol concentration in this period. After that, TH molecules may diffuse through the chitosan matrix more slowly. The nanocapsule size, chitosan crosslinking, and thymol-chitosan chain interactions may have affected this sustained release phase. Finally, the rate of thymol release may have plateaued when a balance was struck between thymol diffusion out of nanocapsules and possible interactions that could slow release. Within 24 hours, chitosan nanoparticles released 58% thymol.

3.5. Biological studies

3.5.1. Cytotoxicity. The study on the cytotoxicity of new materials (TEO, QUCS, NBC1, NBC2), in comparison to a reference drug (ciprofloxacin, CIP), towards Vero E6 cells has provided valuable insights into the potential therapeutic applications of these natural bioactive materials. To that end, we have employed the MTT assay, a widely used method for assessing cell viability by measuring the reduction of yellow tetrazolium salt to purple formazan crystals by mitochondrial dehydrogenases. Additionally, for estimating the half-maximal cytotoxic concentration (CC_{50}), or the concentration that causes a 50% reduction in cell viability, the MTT assay is particularly relevant. By determining the concentration-dependent decrease in cell viability, we can evaluate the cytotoxic potential of these materials on Vero E6 cells. The results of the study (Fig. 7) revealed that the new exhibited low cytotoxic effects on Vero E6 cells in a dose-dependent manner. An infinitesimal decrease in cell viability was observed at low concentrations of these materials. In contrast, a moderate decrease in Vero cell viability occurred at higher concentrations, indicating their low cytotoxic impacts on Vero E6 cells. Meanwhile, the high values of CC_{50} observed for these materials (see Table 2) indicate that they have low cytotoxicity and are well-tolerated by cells. This finding is crucial for developing biocompatible materials that can be used in various biomedical applications. These findings suggest that new materials have the potential to be further explored as a therapeutic agent for the development of antimicrobial coatings or scaffolds in tissue engineering applications.

3.5.2. Anti-SARS-CoV-2 activity. The use of the CC_{50} doses to evaluate the antiviral activity of new materials against SARS-CoV-2 has proven effective.[63] In this context, we have utilized the CC_{50} dosages to evaluate the antiviral activity of the new materials (TEO, QUCS, NBC1, NBC2) against the SARS-CoV-2 virus. The antiviral screening revealed that the new materials exhibited promising *in vitro* activity against SARS-CoV-2. This suggests that they have the potential to inhibit the replication of the virus and potentially serve as effective antiviral agents. Furthermore, the evaluation of the dose-dependent performance of these materials in the antiviral screening highlights their ability to exert antiviral effects in a concentration-dependent style, with higher concentrations of the materials leading to greater inhibition of the virus (see Fig. 8). Amongst the tested samples, thyme oil-loaded quaternized chitosan (NBC1) show the most potent antiviral activity, even higher than that of NBC2 and CIP, against SARS-CoV-2 (IC_{50} = 0.021 μg mL^{-1}, see Table 2). This could be attributed to several factors. Firstly, thyme oil is known for its strong antimicrobial properties, including antiviral activity. It contains various bioactive compounds, such as thymol and carvacrol, which have been shown to exhibit potent antiviral effects against a range of viruses.[64] When loaded into QUCS, the antiviral activity of thyme oil is further enhanced. The positive charge on the surface of quaternized chitosan allows it to interact effectively

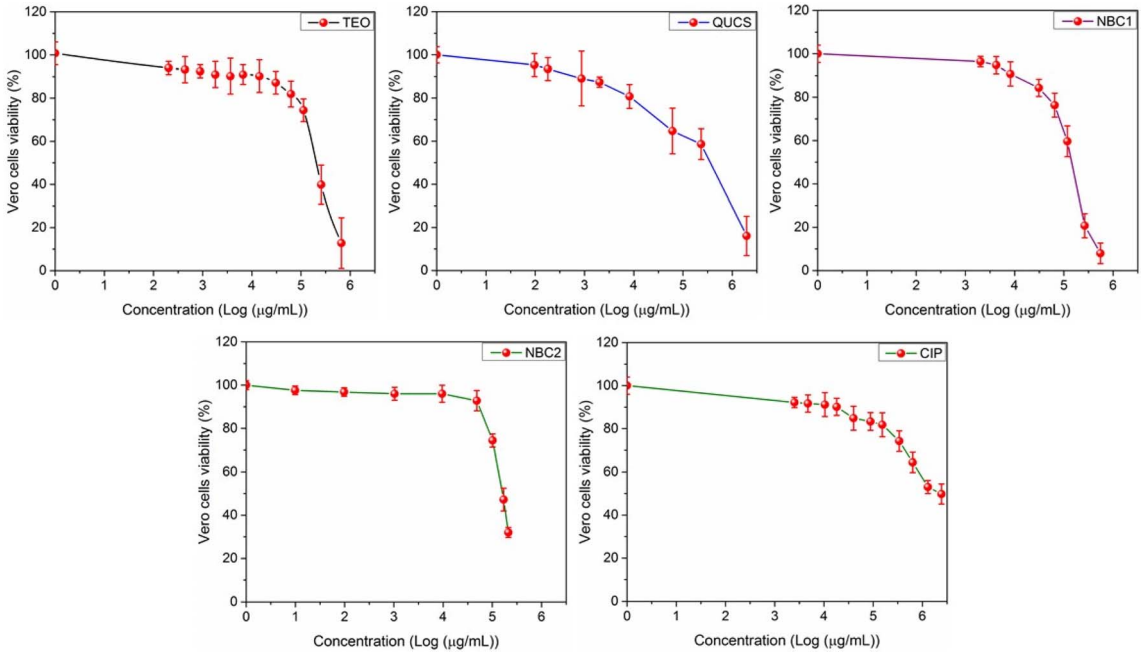

Fig. 7 Effect of serial concentrations of the obtained formulations on the cellular proliferation of Vero E6 cell lines following 24 h of treatment. Values are expressed as the mean ± SD of 3 separate experiments performed in triplicate.

with the negatively charged viral envelope of SARS-CoV-2, thereby disrupting its integrity and inhibiting viral replication. Additionally, the combination of thyme oil and quaternized chitosan may lead to a synergistic effect, where the two components work together to exert a stronger antiviral effect than either compound alone. This could be due to their complementary mechanisms of action, such as thyme oil targeting viral proteins or nucleic acids, while QUCS disrupts the viral envelope.[65] Moreover, the formulation of thyme oil-loaded QUCS as in nanostructures could enhance its antiviral activity by increasing its stability, bioavailability, and targeted delivery to the site of infection. In conclusion, the synergy between thyme oil and quaternized chitosan in NBC1 offers substantial promise as a viable candidate for future antiviral

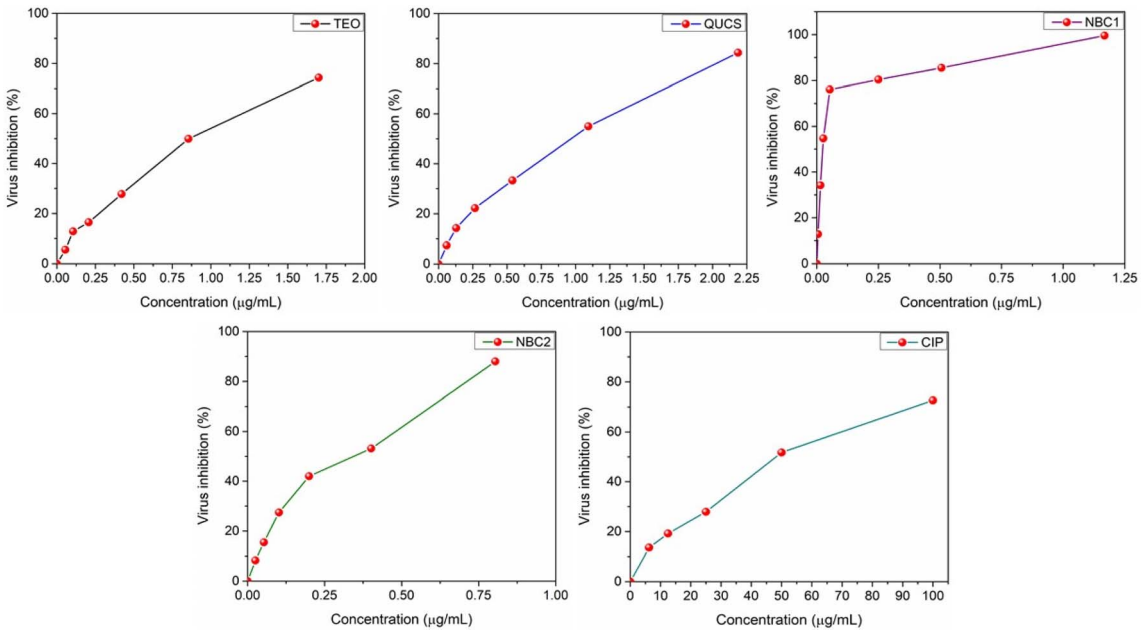

Fig. 8 Effect of serial concentrations of the obtained formulations on the viral proliferation of SARS-CoV-2 following 24 h of treatment. Values are expressed as the mean ± SD of 3 separate experiments performed in triplicate.

strategies targeting SARS-CoV-2. By leveraging the individual strengths of each component while simultaneously fostering beneficial physiological changes, this formulation holds considerable potential in the fight against COVID-19.

3.5.3. Selectivity toward viral over healthy cells. The selectivity index (SI) values play a crucial role in evaluating the potential effectiveness of antiviral treatments. SI values have allowed quantitatively assessing a new material's preferential targeting of viral cells while minimizing harm to healthy cells. SI is calculated by dividing the cytotoxicity of a compound toward healthy cells (CC_{50}) by its antiviral activity (IC_{50}), thus providing insight into the compound's specificity and safety profile. Table 2 shows the results of the calculations, which showed that all of the materials examined had high selectivity index (SI) values. This means they are more selective against viral cells (SARS-CoV-2) and less harmful to host cells (Vero E6). This finding not only highlights the potential of these materials as potential candidates for antiviral therapies but also underscores the importance of selective targeting in developing effective treatment options. The SI value of NBC1 was the highest (SI 5305.77) compared to its nascent ingredients (TEO, SI 203.24 and QUCS, SI 209.52), indicating its superior ability to selectively target and inhibit viral cells while being less toxic to healthy cells.[66] Similarly, the SI value of NBC2 (SI 4278.18) was higher than compared to its active ingredients (TH, SI 2.99 and QUCS, SI 209.52),[67] demonstrating its selectivity to attack viral cells over healthy ones. One of the main reasons for the higher selectivity of our nanocomposites is the synergistic effect of QUCS and TEO.[68] Other important factors to consider are the size and surface charge of the nanocomposites. QUCS, being a cationic polymer, can easily interact with the negatively charged envelope of the virus, leading to its disruption. Finally, the specificity of our nanocomposites may be due to the fact that TEO is released from the QUCS matrix under regulated conditions. A sustained release of the chemical, made possible by encapsulating it within the QUCS matrix, guarantees a persistent antiviral impact.[69] As such, these findings pave the way for further research and exploration into the utilization of this nanobiocomposite in the battle against viral infections, offering hope for the development of safer and more targeted approaches to combat the ongoing pandemic and future viral outbreaks.

3.5.4. Plaque reduction assay. The plaque reduction assay (PRA) plays a crucial role in evaluating the effectiveness of new antiviral agents. PRA involves the quantification of visible plaques formed by viral infection in cell monolayers and subsequent measurement of the reduction in plaque formation in the presence of antiviral compounds. This assay provides valuable information about the ability of antiviral agents to inhibit viral replication and spread, and it has been extensively employed in the development and screening of antiviral drugs. The significance of PRA lies in its ability to accurately determine the antiviral activity of compounds by directly assessing their impact on viral infectivity.[70] As represented in Fig. 9, all materials showed exceptionally high activities against the SARS-CoV-2 virus. It was observed that the effectiveness of these materials was dependent on their specific structural properties. The nanobiocomposites (NBC1 and NBC2) exhibited the highest level of activity among the tested samples in inhibiting the replication of the virus, with inhibition percentages of 84.6% and 80.1%, respectively. In contrast, the native ingredients (TEO and QUCS) show lower levels of antiviral activity, with inhibition percentages of 75.7% and 70.8%, respectively. These findings demonstrated that the encapsulation of thyme oil with quaternized chitosan significantly enhances its antiviral activity against SARS-CoV-2. This synergistic effect can be attributed to the unique properties and mechanisms of thyme oil and quaternized chitosan. The encapsulation process provides protection against degradation, sustained release of active compounds, and improved stability and solubility of thyme oil. Moreover, the positively charged quaternary ammonium groups of quaternized chitosan can interact with the negatively charged viral envelope, disrupting its integrity and preventing viral entry into host cells.[65] This promising approach opens up possibilities for the development of novel antiviral formulations that can effectively combat SARS-CoV-2 and other viral infections.

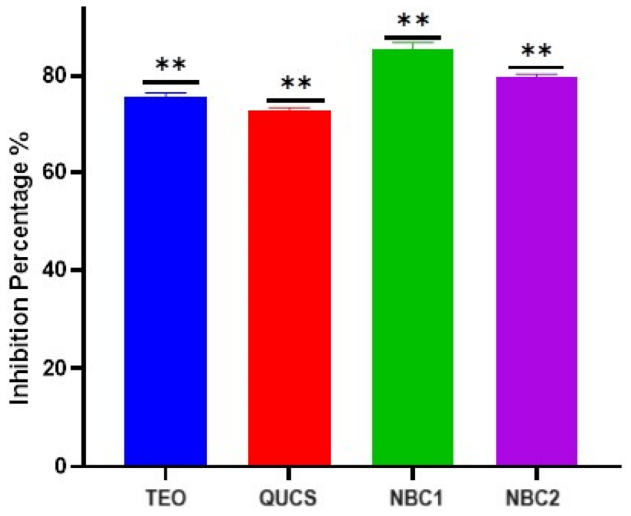

Fig. 9 The proportion of viral inhibition across all samples examined. The data is summarized as means ± SD ($n = 2$) with a p-value less than 0.0001.

4 Conclusion

O-Quaternized ultrasonic deacetylated chitosan (QUCS) was successfully prepared and used to encapsulate the extracted TEO or TH using Tween 80, creating nanobiocomposites (NBCs; NBC1 and NBC2, respectively). Encapsulating these natural therapeutic materials has improved their effectiveness, targeted delivery, bioavailability, and stability. Interestingly, results of the *in vitro* antiviral studies demonstrate the potential of these NBCs as promising candidates for anti-COVID treatments and emphasize their specificity in targeting SARS-CoV-2. The ideal pharmacokinetic properties (sustained- and controlled-release) of these NBCs coupled with their superior antiviral activity make them promising candidates for future antiviral therapies. Our future study will focus on a multimodal strategy that

includes *in vitro*, *in vivo*, and computational investigations to fully examine the efficiency of nanocomposites and their bioactive components as antiviral medicines against SARS-CoV-2 and other viral infections. *In vitro* investigations will allow for a more controlled examination of cellular interactions, revealing early insights into the antiviral mechanisms at work. Concurrently, *in vivo* investigations will be critical for understanding how these nanocomposites behave in complex biological systems, revealing possible therapeutic windows and any detrimental consequences that may occur. Furthermore, using computer modeling to simulate molecular interactions with virus particles and human cells can help identify promising nanocomposite formulations more quickly. By combining data from several different approaches, we hope to not only identify the molecular pathways by which these nanocomposites exercise their antiviral activities, but also optimize their design for maximum performance and safety. This thorough investigation is necessary for establishing effective therapeutic strategies to tackle present and emerging viral threats.

Data availability

The data that support the findings of this study are available from the corresponding author upon reasonable request.

Conflicts of interest

The authors declare that they have no known competing financial interests or personal relationships that could have appeared to influence the work reported in this paper.

References

1 F. K. Ayittey, B. K. Dhar, G. Anani and N. B. Chiwero, *Health Care Women Int.*, 2020, **41**, 1210–1225.
2 M. Maher and L. Owens, *Best Pract. Res. Clin. Endocrinol. Metabol.*, 2023, 101760.
3 M. Cox, T. P. Peacock, W. T. Harvey, J. Hughes, D. W. Wright, C.-G. U. Consortium, B. J. Willett, E. Thomson, R. K. Gupta and S. J. Peacock, *Nat. Rev. Microbiol.*, 2023, **21**, 112–124.
4 S. Iketani, H. Mohri, B. Culbertson, S. J. Hong, Y. Duan, M. I. Luck, M. K. Annavajhala, Y. Guo, Z. Sheng and A.-C. Uhlemann, *Nature*, 2023, **613**, 558–564.
5 S. Drożdżal, J. Rosik, K. Lechowicz, F. Machaj, B. Szostak, J. Przybyciński, S. Lorzadeh, K. Kotfis, S. Ghavami and M. J. Łos, *Drug Resistance Updates*, 2021, **59**, 100794.
6 D. Giordano, A. Facchiano and V. Carbone, *Molecules*, 2023, **28**, 2470.
7 S. A. Heleno, M. Carocho, F. S. Reis, T. C. S. P. Pires, M. Pintado, I. C. F. R. Ferreira and L. Barros, *Life*, 2023, **13**, 386.
8 T.-H. Chen, M.-J. Tsai, C.-S. Chang, L. Xu, Y.-S. Fu and C.-F. Weng, *J. Infect. Public Health*, 2023, **16**, 42–54.
9 W. Abd El-Fattah, M. Y. Alfaifi, J. Alkabli, H. A. Ramadan, A. A. Shati, S. E. I. Elbehairi, R. F. M. Elshaarawy, I. Kamal and M. M. Saleh, *Antibiotics*, 2023, **12**, 1110.
10 Ö. Adem, O. ÖZbek and S. Nached, *J. Turk. Chem. Soc., Sect. A*, 2020, **7**, 821–826.
11 R. Rolta, D. Salaria, P. Sharma, B. Sharma, V. Kumar, B. Rathi, M. Verma, A. Sourirajan, D. J. Baumler and K. Dev, *Curr. Pharmacol. Rep.*, 2021, **7**, 135–149.
12 H. M. Mengist, Z. Khalid and F. Adane, *Adv. Appl. Bioinf. Chem.*, 2023, 1–13.
13 A. Kowalczyk, M. Przychodna, S. Sopata, A. Bodalska and I. Fecka, *Molecules*, 2020, **25**, 4125.
14 Ç. Şakalar and M. Ertürk, *J. Virol. Methods*, 2023, **312**, 114660.
15 S. K. Sundar and J. K. Parikh, *Int. J. Pharm.*, 2023, 122668.
16 Q. Guo, G. Du, H. Jia, Q. Fan, Z. Wang, Z. Gao, T. Yue and Y. Yuan, *Food Biosci.*, 2021, **44**, 101367.
17 Y. Yang, M. Aghbashlo, V. K. Gupta, H. Amiri, J. Pan, M. Tabatabaei and A. Rajaei, *Int. J. Biol. Macromol.*, 2023, 123954.
18 G. Granata, S. Stracquadanio, M. Leonardi, E. Napoli, G. Malandrino, V. Cafiso, S. Stefani and C. Geraci, *Molecules*, 2021, **26**, 4055.
19 M. Sotelo-Boyás, Z. Correa-Pacheco, S. Bautista-Baños and Y. G. y Gómez, *Int. J. Biol. Macromol.*, 2017, **103**, 409–414.
20 M. Ghaderi-Ghahfarokhi, M. Barzegar, M. A. Sahari and M. H. Azizi, *Food Bioprocess Technol.*, 2016, **9**, 1187–1201.
21 M. Barzegar, M. Ghaderi Ghahfarokhi, M. A. Sahari and M. H. Azizi, *J. Agric. Sci. Technol.*, 2016, **18**, 1781–1792.
22 P. Gupta, S. Preet and N. Singh, *Sci. Rep.*, 2022, **12**, 1–14.
23 H. Hamedi, S. Moradi, A. E. Tonelli and S. M. Hudson, *Appl. Sci.*, 2019, **9**, 3933.
24 A. Giannakas, P. Stathopoulou, G. Tsiamis and C. Salmas, *J. Food Process. Preserv.*, 2020, **44**, e14327.
25 S. Moradi, A. Barati, A. E. Tonelli and H. Hamedi, *Eur. Polym. J.*, 2020, **122**, 109303.
26 A. Zehra, S. M. Wani, T. A. Bhat, N. Jan, S. Z. Hussain and H. R. Naik, *Int. J. Biol. Macromol.*, 2022, **217**, 572–582.
27 R. Zhao, J. Chen, S. Yu, R. Niu, Z. Yang, H. Wang, H. Cheng, X. Ye, D. Liu and W. Wang, *Food Hydrocolloids*, 2023, **134**, 108094.
28 M. Hassani and S. Hasani, *Trends Phytochem. Res.*, 2018, **2**, 75–82.
29 J. Sheorain, M. Mehra, R. Thakur, S. Grewal and S. Kumari, *Int. J. Biol. Macromol.*, 2019, **125**, 1069–1074.
30 A. M. Nasr, Y. I. Mortagi, N. H. A. Elwahab, M. Y. Alfaifi, A. A. Shati, S. E. I. Elbehairi, R. F. M. Elshaarawy and I. Kamal, *Pharmaceutics*, 2022, **14**, 1350.
31 S. E. I. Elbehairi, L. A. Ismail, M. Y. Alfaifi, R. F. M. Elshaarawy and H. S. Hafez, *Int. J. Biol. Macromol.*, 2020, **165**, 2750–2764.
32 R. F. M. Elshaarawy, H. R. Z. Tadros, R. M. Abd El-Aal, F. H. A. Mustafa, Y. A. Soliman and M. A. Hamed, *J. Environ. Chem. Eng.*, 2016, **4**, 2754–2764.
33 R. F. M. Elshaarawy and C. Janiak, *Tetrahedron*, 2014, **70**, 8023–8032.
34 R. F. M. Elshaarawy, I. M. Eldeen and E. M. Hassan, *J. Mol. Struct.*, 2017, **1128**, 162–173.

35 I. Kamal, A. I. M. Khedr, M. Y. Alfaifi, S. E. I. Elbehairi, R. F. M. Elshaarawy and A. S. Saad, *Int. J. Biol. Macromol.*, 2021, **188**, 523–533.
36 Egyptian Pharmacopoeia, *Administration and Pharmaceutical Affairs*, Ministry of Health and Population, Cairo, Egypt, 4th edn, 2005.
37 D. Villanueva Bermejo, I. Angelov, G. Vicente, R. P. Stateva, M. Rodriguez García-Risco, G. Reglero, E. Ibañez and T. Fornari, *J. Sci. Food Agric.*, 2015, **95**, 2901–2907.
38 C.-H. Wang, W.-S. Liu, J.-F. Sun, G.-G. Hou, Q. Chen, W. Cong and F. Zhao, *Int. J. Biol. Macromol.*, 2016, **84**, 418–427.
39 A. Wan, Q. Xu, Y. Sun and H. Li, *J. Agric. Food Chem.*, 2013, **61**, 6921–6928.
40 Z. Li, F. Yang and R. Yang, *Int. J. Biol. Macromol.*, 2015, **75**, 378–387.
41 J. Huang, Z.-H. Cheng, H.-H. Xie, J.-Y. Gong, J. Lou, Q. Ge, Y.-J. Wang, Y.-F. Wu, S.-W. Liu, P.-L. Sun and J.-W. Mao, *Int. J. Biol. Macromol.*, 2014, **70**, 545–550.
42 O. M. Hendawy, M. M. Al-Sanea, R. M. Elbargisy, H. U. Rahman, A. A. B. Mohamed, I. Kamal, R. F. M. Elshaarawy, A. I. M. Khedr and W. A. El-Fattah, *Pharmaceutics*, 2022, **15**, 81.
43 A. M. Nasr, Y. I. Mortagi, N. H. A. Elwahab, M. Y. Alfaifi, A. A. Shati, S. E. I. Elbehairi, R. F. Elshaarawy and I. Kamal, *Pharmaceutics*, 2022, **14**, 1350.
44 A. Mostafa, A. Kandeil, Y. A. M. M. Elshaier, O. Kutkat, Y. Moatasim, A. A. Rashad, M. Shehata, M. R. Gomaa, N. Mahrous, S. H. Mahmoud, M. GabAllah, H. Abbas, A. E. Taweel, A. E. Kayed, M. N. Kamel, M. E. Sayes, D. B. Mahmoud, R. El-Shesheny, G. Kayali and M. A. Ali, *Pharmaceuticals*, 2020, **13**, 443.
45 S. Payne, *Viruses*, ed. S. Payne, Academic Press, 2017, pp. 37–52, DOI: 10.1016/B978-0-12-803109-4.00004-0.
46 Y. Zhang, M. Yang, N. G. Portney, D. Cui, G. Budak, E. Ozbay, M. Ozkan and C. S. Ozkan, *Biomed. Microdevices*, 2008, **10**, 321–328.
47 A. M. Nasr, S. M. Aboelenin, M. Y. Alfaifi, A. A. Shati, S. E. I. Elbehairi, R. F. M. Elshaarawy and N. H. A. Elwahab, *Pharmaceutics*, 2022, **14**, 1319.
48 A. A. Refaee, M. E. El-Naggar, T. B. Mostafa, R. F. M. Elshaarawy and A. M. Nasr, *Eur. Polym. J.*, 2022, **166**, 111040.
49 R. Batool, S. Ayub and I. Akbar, *Soil Environ.*, 2017, **36**, 35–44.
50 P. Gupta, S. Preet, S. N. Ananya and N. Singh, *Sci. Rep.*, 2022, **12**, 4335.
51 X. Wang, Y. Hu, Z. Zhang and B. Zhang, *J. Cult. Herit.*, 2022, **53**, 206–211.
52 O. M. Hendawy, M. M. Al-Sanea, R. M. Elbargisy, H. U. Rahman, Y. A. Hassan, R. F. M. Elshaarawy and A. I. M. Khedr, *Int. J. Pharm.*, 2023, **643**, 123260.
53 J. Cai, Q. Dang, C. Liu, T. Wang, B. Fan, J. Yan and Y. Xu, *Int. J. Biol. Macromol.*, 2015, **80**, 8–15.
54 J. Kaur, A. Kour, J. J. Panda, K. Harjai and S. Chhibber, *AAPS PharmSciTech*, 2020, **21**, 233.
55 M. E. Sotelo-Boyás, G. Valverde-Aguilar, M. Plascencia-Jatomea, Z. N. Correa-Pacheco, A. Jiménez-Aparicio, J. Solorza-Feria, L. Barrera-Necha and S. Bautista-Baños, *Rev. Mex. Ing. Quim.*, 2015, **14**, 589–599.
56 D. Dinesh, K. Murugan, J. Subramaniam, M. Paulpandi, B. Chandramohan, K. Pavithra, J. Anitha, M. Vasanthakumaran, L. F. Fraceto, L. Wang, J. Shoiu-Hwang and H.-U. Dahms, *Biopesticides*, eds. A. Rakshit, V. S. Meena, P. C. Abhilash, B. K. Sarma, H. B. Singh, L. Fraceto, M. Parihar and A. K. Singh, Woodhead Publishing, 2022, pp. 159–181, DOI: 10.1016/B978-0-12-823355-9.00022-5.
57 G. Midekessa, K. Godakumara, J. Ord, J. Viil, F. Lättekivi, K. Dissanayake, S. Kopanchuk, A. Rinken, A. Andronowska and S. Bhattacharjee, *ACS Omega*, 2020, **5**, 16701–16710.
58 X. Zhang, B. B. Ismail, H. Cheng, T. Z. Jin, M. Qian, S. A. Arabi, D. Liu and M. Guo, *Carbohydr. Polym.*, 2021, **273**, 118616.
59 H. Chen, Y. Zhang and Q. Zhong, *J. Food Eng.*, 2015, **144**, 93–102.
60 J. Yammine, A. Gharsallaoui, A. Fadel, L. Karam, A. Ismail and N.-E. Chihib, *J. Drug Delivery Sci. Technol.*, 2023, **84**, 104443.
61 P. Gutiérrez-González, L. Fernández-Peña, A. Lucia, F. Ortega, R. G. Rubio and E. Guzmán, *Colloids Surf., A*, 2024, **690**, 133775.
62 M. Vehapi, A. Yilmaz and D. Özçimen, *J. Nat. Fibers*, 2021, **18**, 1359–1373.
63 R. Alaaeldin, M. Mustafa, G. E. D. A. Abuo-Rahma and M. Fathy, *Fundam. Clin. Pharmacol.*, 2022, **36**, 160–170.
64 A. Kowalczyk, M. Przychodna, S. Sopata, A. Bodalska and I. Fecka, *Molecules*, 2020, **25**, 4125.
65 A. Teotia, I. Laurén, S. Borandeh and J. Seppälä, *ACS Appl. Mater. Interfaces*, 2023, **15**, 18707–18719.
66 D. B. Mahmoud, M. M. Bakr, A. A. Al-Karmalawy, Y. Moatasim, A. El Taweel and A. Mostafa, *AAPS PharmSciTech*, 2022, **23**, 1–12.
67 M. G. Seadawy, A. F. Gad, M. F. Elhoseny, B. E. Elharty, M. D. Shamel, A. A. Elfiky, A. Ahmed and A. R. N. Zekri, *bioRxiv*, 2020, **11**, 367649.
68 N. Iraci, C. Corsaro, S. V. Giofrè, G. Neri, A. M. Mezzasalma, M. Vacalebre, A. Speciale, A. Saija, F. Cimino and E. Fazio, *Biomolecules*, 2022, **12**, 1060.
69 F. A. M. Abdelgawad, S. S. El-Hawary, E. M. Abd El-Kader, S. A. Alshehri, M. A. Rabeh, A. E. M. K. El-Mosallamy, M. A. El Raey and R. A. El Gedaily, *Plants*, 2023, **12**, 2813.
70 A. Maeda and J. Maeda, *Vet. J.*, 2013, **195**, 33–40.